

In Situ Visualization of Structural Evolution and Fissure Breathing in (De)lithiated $\text{H}_2\text{V}_3\text{O}_8$ Nanorods

Yi Wu,^{†,‡} Xiaoming Xu,^{†,‡} Chongyang Zhu,^{†,‡} Pengcheng Liu,[§] Shize Yang,^{||} Huolin L. Xin,[⊥] Ran Cai,[†] Libing Yao,[†] Meng Nie,[†] Shuangying Lei,[†] Peng Gao,[∇] Litao Sun,^{*,†} Liqiang Mai,^{*,†} and Feng Xu^{*,†}

[†]SEU-FEI Nano–Pico Center, Key Laboratory of MEMS of Ministry of Education, Southeast University, Nanjing 210096, China

[‡]State Key Laboratory of Advanced Technology for Materials Synthesis and Processing, Wuhan University of Technology, Hubei, Wuhan 430070, China

[§]Texas Materials Institute, The University of Texas at Austin, Austin, Texas 78712, United States

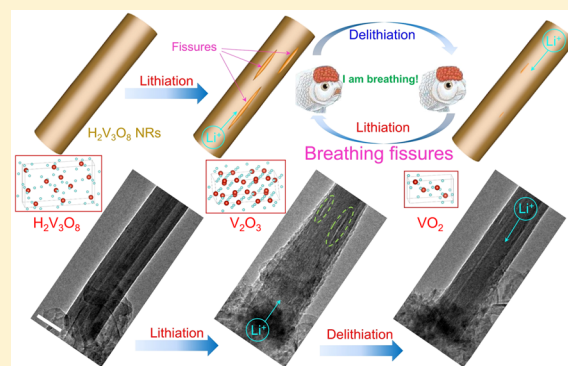
^{||}Center for Functional Nanomaterials, Brookhaven National Laboratory, Upton, New York 11973, United States

[⊥]Department of Physics and Astronomy, University of California, Irvine, California 94720, United States

[∇]Electron Microscopy Laboratory, and International Centre for Quantum Materials, School of Physics, Peking University, Beijing 100871, China

S Supporting Information

ABSTRACT: Layered $\text{H}_2\text{V}_3\text{O}_8$ material consisting of V_3O_8 layers features the elastic space for buffering volume change upon repeated ion (de)intercalations. However, its ion transport and phase transformations still remain largely unknown due to lack of direct evidence. Here we employ in situ transmission electron microscopy to revisit this material carefully. Upon lithiation, the localized phase transformation from $\text{H}_2\text{V}_3\text{O}_8$ to V_2O_3 via an intermediate VO_2 phase was observed, and large structural fissures gradually formed. Unexpectedly, the large fissures were able to self-heal during delithiation with the VO_2 phase as the delithiated product. The fissures could appear and disappear alternately upon subsequent (de)lithiation, in which a stable and reversible phase transformation between V_2O_3 and VO_2 phases was established. These unreported findings are expected to call for renewed attention to this electrode material for a more comprehensive understanding in rechargeable metal-ion batteries.



Rechargeable lithium-ion batteries (LIBs) currently dominate the portable electronic product market because of their high energy density and superior cycle life.^{1–5} However, the increasing demands for electric vehicles and strategic layout of the energy grid have forced us to develop low-cost and high-performance LIBs.^{6–9} In this regard, vanadium oxides have been considered promising electrode materials in LIBs due to their high theoretical capacity and abundant mineral sources.^{10–14} Especially, vanadium oxide $\text{H}_2\text{V}_3\text{O}_8$ with mixed valence and good electronic conductivity has attracted great concern.^{15–19} The crystal structure of $\text{H}_2\text{V}_3\text{O}_8$ consists of V_3O_8 layers stacked along the *a*-axis, thus affording interlayer vacant sites (Figure S1, Supporting Information). The V_3O_8 layers are interlinked by hydrogen bonds; each V_3O_8 layer is composed of VO_6 octahedra and VO_5 trigonal bipyramids. VO_6 octahedra share

corners with edge-sharing VO_5 trigonal bipyramids and share edges with neighboring ones stacked along the *c*-axis, forming a two-dimensional slab in the *bc*-plane.^{20,21} Adjacent V_3O_8 layers are connected by hydrogen bonds. Benefiting from hydrogen bond vibrations, such V_3O_8 layers possess elastic spaces for buffering volume change. Additionally, V^{5+} and V^{4+} exist together in $\text{H}_2\text{V}_3\text{O}_8$ with a ratio of 2:1, resulting in a reduced mixed valence (+4.67) that contributes to high electrical conductivity.^{22–25} Moreover, the large interlayer spacing (~ 8.5 Å) between V_3O_8 layers can accommodate larger charge carriers than Li ions. With these merits, $\text{H}_2\text{V}_3\text{O}_8$ has shown its

Received: June 27, 2019

Accepted: August 7, 2019

Published: August 7, 2019

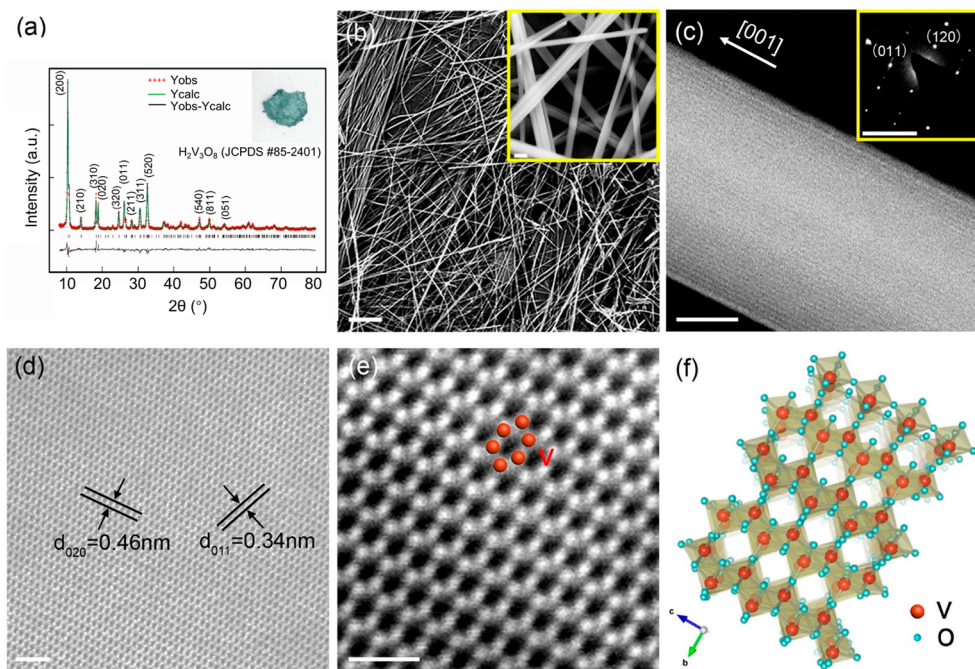


Figure 1. (a) XRD pattern and an optical image of as-prepared $\text{H}_2\text{V}_3\text{O}_8$ NRs. Rietveld refinement showing data points (Yobs, red cross) and the calculated profile (Ycalc, green line); the difference profile (black line) is indicated. (b) SEM images of the synthesized $\text{H}_2\text{V}_3\text{O}_8$ NRs. Scale bars, 5 μm and 200 nm. (c) STEM images of the $\text{H}_2\text{V}_3\text{O}_8$ NR with an inset of the SAED pattern. Scale bars, 10 nm and 5 1/nm. (d,e) STEM images of the $\text{H}_2\text{V}_3\text{O}_8$ NR. Scale bars, 2 and 1 nm, respectively. (f) Crystal structure of $\text{H}_2\text{V}_3\text{O}_8$ viewed along the [100] direction.

potential as an intercalation electrode for lithium-, sodium-, zinc-, and magnesium-ion batteries.^{26–29}

Although the intercalation mechanism associated with the layered structure of $\text{H}_2\text{V}_3\text{O}_8$ has been well documented in various batteries, the structural advantage has still not been fully understood due to lack of direct evidence. Particularly, the dynamics of ionic transport and phase evolutions in such a structure still remains largely unknown. Unlike the bulk-based techniques (e.g., in situ X-ray diffraction and absorption spectroscopy) that gather global information from bulk materials or ex situ techniques that are subjected to potential sample contamination, the recently developed in situ transmission electron microscopy (TEM) approach with higher spatial and temporal resolution can directly observe the localized microstructure and phase evolutions down to the atomic scale within a short time scale.^{30–34} Thus, the in situ TEM technique can provide supporting information that cannot be obtained by the ex situ or bulk-based techniques. Nanoscale and even atomic-scale visualization evidence has achieved great success in understanding underlying reasons behind new phenomena discovered recently in the field of battery research.

Herein, we employed an ensemble of in situ TEM approaches, including high-resolution imaging, localized electron diffraction (ED), and electron energy loss spectroscopy (EELS), to revisit the $\text{H}_2\text{V}_3\text{O}_8$ material during (de)lithiation. Real-time tracking of ion insertion and extraction processes in well-crystallized $\text{H}_2\text{V}_3\text{O}_8$ nanorods (NRs) was carried out by in situ TEM observation. Upon lithiation, the $\text{H}_2\text{V}_3\text{O}_8$ NRs undergo a localized phase transition from pristine $\text{H}_2\text{V}_3\text{O}_8$ to the V_2O_3 phase via an intermediate phase VO_2 , as confirmed by the ED patterns. As the lithiation advances, structural fissures begin to occur and gradually extend, with their length directions basically parallel to the NR axes. The fissures that were considered an omen of irreversible structural

degradation in previous reports are able to self-heal here upon subsequent delithiation. Interestingly, the fissures can appear and disappear repeatedly during multiple lithiation/delithiation processes, which is like breathing. Therefore, we, for the first time, name the observed self-healing of the fissures “fissure breathing”. Obviously, this phenomenon subverts a commonly accepted understanding, that is, the serious structural degradation in electrode materials is basically irreversible. These findings in the present work are expected to attract more attention to this material for a precise structure–property relationship, particularly toward achieving advanced functional batteries.

The phase purity of the as-synthesized material has been confirmed by Rietveld refinement of the X-ray diffraction (XRD) pattern, as shown in Figure 1a. The corresponding refinement parameters are presented in Table S1. All of the peaks can be well indexed to the orthorhombic $\text{H}_2\text{V}_3\text{O}_8$ (JCPDS No. 85-2401, space group: $Pnam$, $a = 16.9298$ Å, $b = 9.3598$ Å, $c = 3.6443$ Å), which indicates the high purity of the sample. The sharp diffraction peaks reflect good crystallinity of $\text{H}_2\text{V}_3\text{O}_8$ NRs, and the low-angle (200) peak reveals a large interlamellar spacing of about 8.5 Å.³⁵ A photograph of the $\text{H}_2\text{V}_3\text{O}_8$ sample is inset in Figure 1a. The morphology of the sample is observed by SEM and STEM, as shown in Figure 1b–e. A one-dimensional rod-like shape with a smooth surface is identified to grow along the [001] direction. The NRs are several micrometers in length and around 100 nm in diameter. The ED pattern in Figure 1c reveals the monocrystalline feature of the $\text{H}_2\text{V}_3\text{O}_8$ NRs. The STEM image in Figure 1d shows ordered lattice fringes of 0.46 and 0.34 nm, corresponding to (020) and (011) planes of $\text{H}_2\text{V}_3\text{O}_8$, respectively.

Further, the atomic-resolution STEM image in Figure 1e clearly identifies the quasi-hexagon arrangement of the V atom column (marked with red dots), matching well with the atomic

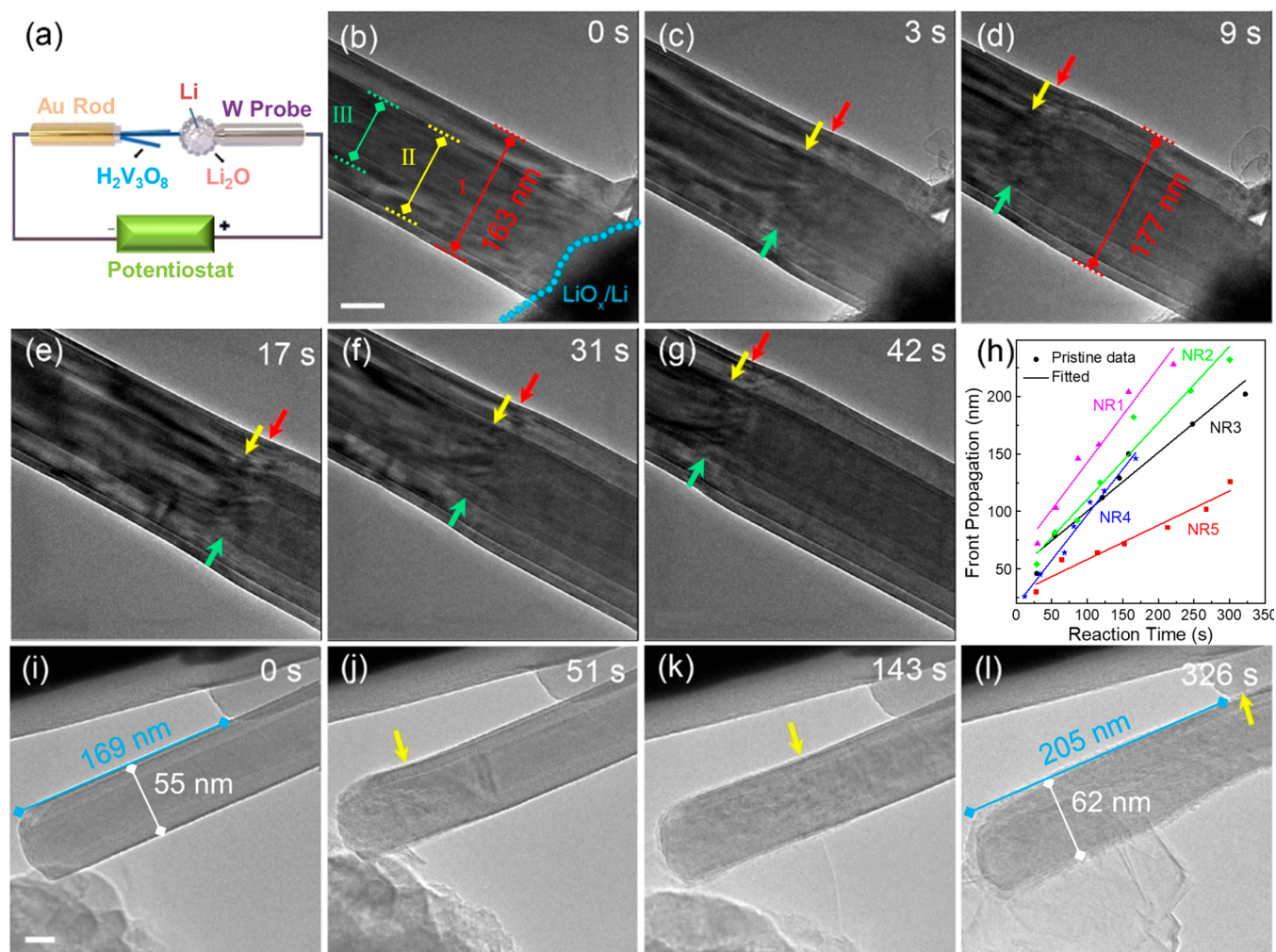


Figure 2. (a) Schematic illustration of the experimental setup for in situ electrochemical lithiation/delithiation. (b–g;i–l) Snapshots of different $\text{H}_2\text{V}_3\text{O}_8$ NRs in the lithiation process, showing the longitudinal propagation of a RF (marked by red, yellow, and green arrows) followed by a diametral expansion of the lithiated region. Scale bars, 50 and 20 nm, respectively. (h) Propagation length of the RF plotted as a function of time.

structure model of $\text{H}_2\text{V}_3\text{O}_8$ consisting of VO_6 octahedra and VO_5 trigonal bipyramids, as illustrated in Figure 1f. Two VO_6 octahedra are piled up along the c -axis by sharing edges and are connected by two edge-shared VO_5 trigonal bipyramids along the b -axis, forming a V_3O_8 layer along the a -axis.³⁵ In addition, hydrogen atoms are bonded to oxygen atoms labeled O(6) in VO_6 octahedra, forming hydrogen bonds and holding V_3O_8 layers, thus yielding a 3D structure. These special hydrogen bonds can buffer the structure expansion/contraction when the ions insert into or extract from the interlamination of $\text{H}_2\text{V}_3\text{O}_8$.^{28,35,36} The valence state of the vanadium is further investigated by X-ray photoelectron spectroscopy (XPS) in Figure S2 (Supporting Information). Two asymmetrical peaks, corresponding to $\text{V } 2p_{3/2}$ and $\text{V } 2p_{1/2}$ orbitals, respectively, can be clearly observed at 518 and 525 eV. The $\text{V } 2p_{3/2}$ can further be divided into two different peaks of V^{4+} (516.3 eV) and V^{5+} (517.9 eV). By fitting the curve, the $\text{V}^{5+}/\text{V}^{4+}$ ratio is calculated to be 2.03, very close to the theoretical value 2.00 of the $\text{V}^{5+}/\text{V}^{4+}$ ratio in $\text{H}_2\text{V}_3\text{O}_8$.^{37,38}

The all-solid nanosized LIBs that enable the real-time observation of the in situ (de)lithiation process of samples were constructed inside of a TEM, as schematically shown in Figure 2a. The morphology evolution observed experimentally

during (de)lithiation of $\text{H}_2\text{V}_3\text{O}_8$ NRs is sampled by a series of still images. Figure 2b shows three overlapped NRs (termed I, II, and III) that contacted directly with the Li resource. Thus, we were able to observe nearly synchronous lithium transport for the three NRs, as shown in Movie S1 in the Supporting Information. Upon applying a potential, lithium transport in the NRs propagated along the longitudinal direction starting from the point of contact with the Li resource. We observed obvious changes in the interior contrast of NRs where the flowing strain reaction fronts (RFs) began to occur. After 3 s, three distinct lithiation strain reaction fronts (RFs, marked with red, yellow, and green arrows, respectively) appeared, specifically characterized by slight cross-sectional expansion, and propagated longitudinally (Figure 2c), while the regions behind them underwent a radial expansion of around 8.15% (from 163 to 177 nm, from 118 to 128 nm, and from 91 to 99 nm, respectively). Subsequently, the RFs advanced shoulder to shoulder at an equal speed, as shown in Figure 2d–f. At 42 s, the RFs propagated 365 nm within 39 s, corresponding to a speed of 9.36 nm s^{-1} (Figure 2g). Interpreting this as a lower-bound diffusivity (D) implied a value of $\sim 1.7 \times 10^{-15} \text{ m}^2 \text{ s}^{-1}$ based on the Einstein–Smoluchowski relation, $D = L^2/2t$.³⁹ Although there could be a higher diffusivity of Li^+ ahead of the RF, the

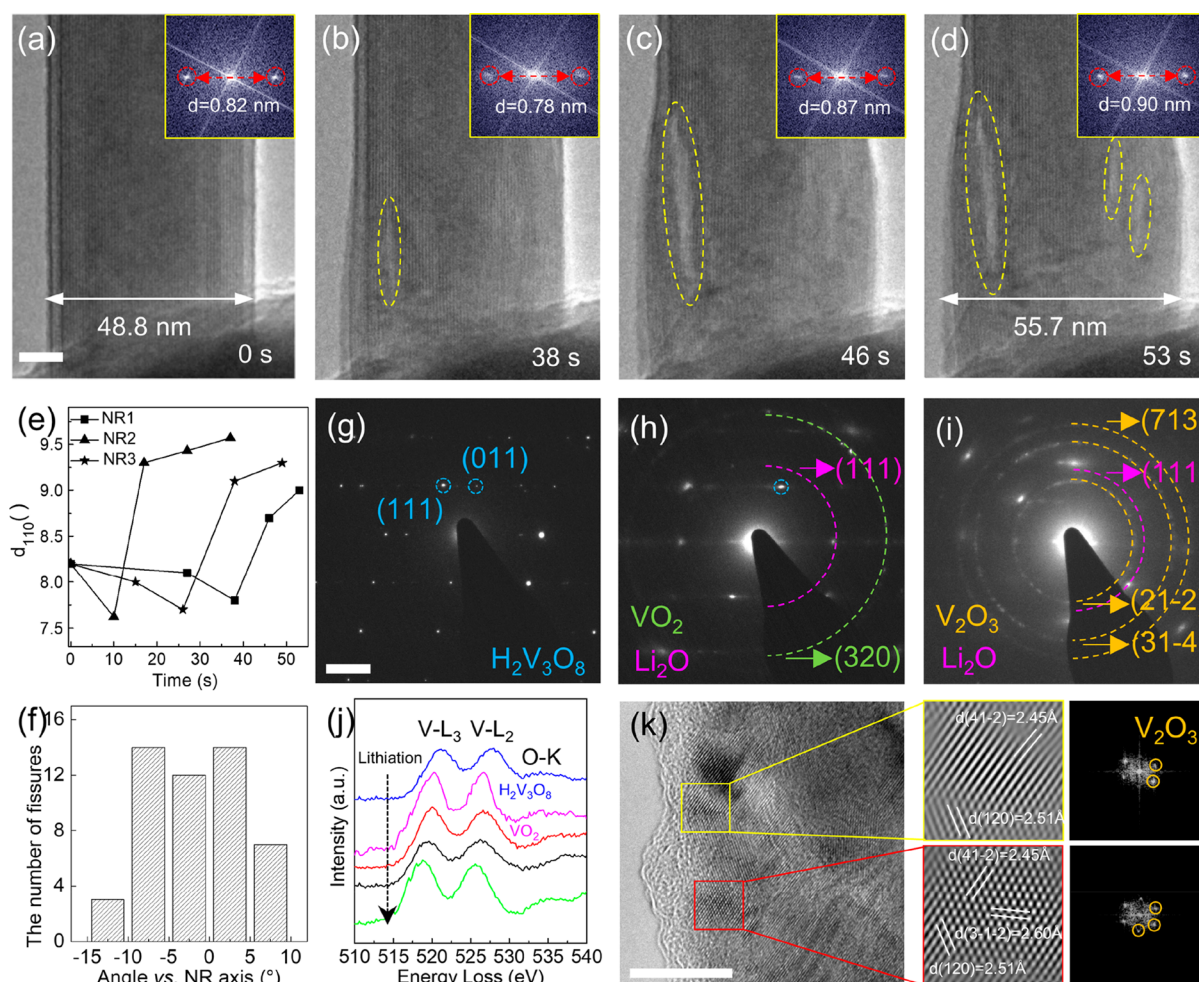


Figure 3. (a–d) HRTEM images of the lithiation process from a video with an inset of the corresponding FFT patterns. The yellow outlines highlight the visible fissure domains upon the lithiation process. (e) Interplanar spacing of the (110) (d_{110}) value variation in the lithiation process. (f) Distribution statistics of the angle between the fissure and NR axis. (j) EELS spectra of V/L_{3,2} edges in the first lithiation process. (g–i) ED patterns used for identifying the phase evolution in the first electrochemical lithiation process. (k) Ex situ TEM images and corresponding FFT patterns of H₂V₃O₈ at the lithiation state at 100 mA g⁻¹. Scale bars, (a–d) 10 nm, (g–i) 2 1/nm, and (k) 10 nm.

value is difficult to judge only via TEM imaging contrast. For the regions of the NRs behind the RFs, the image contrast exhibited totally different appearance from that before the RFs. This observation confirms that the observed morphological changes were due to electrochemical lithiation rather than electron beam-induced phase decomposition, as corroborated by repeated careful in situ experiments (Figure S3 in the Supporting Information).

To probe the dynamics of lithium-ion transport in H₂V₃O₈ NRs, the RF displacements of several NRs are plotted as a function of time, Figure 2h. All curves show linear correlation, indicating that the RF motion of each NR during lithiation is characterized by isokinetic lithium diffusion. We also notice different diffusivities for these NRs, and the average moving speed of these RFs is measured to be $\sim 1\text{--}10\text{ nm s}^{-1}$. Different diffusivities are possibly attributed to the differences in the electrode contact and the local Li⁺ concentration.³³ Moreover, the longitudinal elongation of a NR during lithiation can be estimated quantitatively in Figure 2i–l (Movie S2, Supporting Information). The pristine NR was elongated from 169 to 205 nm within 326 s, corresponding to a longitudinal elongation of 21.30%, as a result of the insertion of lithium ions into the NR (note that the thickness of the Li₂O layer on the surface of the

NR was not included in the estimation). Given that there is a Li concentration gradient along the NR, the actual value may be higher than 21.30%. The irregular Li₂O bubbles observed in the lower left portion of the NR in Figure 2l can be induced by the fast diffusion of Li species along the NR, which is the inherent phenomenon of the in situ TEM experiments.^{32,40} The formation and propagation of Li₂O bubbles are only within a limited distance and would not affect the intrinsic electrochemical reaction. Note that the resulting radial expansion (12.72%) of the NR is essentially the same as that observed for NRs I–III in Figure 2b–g, suggesting their similar lithiation levels.

More detailed structural and phase evolution of H₂V₃O₈ NRs during the first lithiation process are further tracked by HRTEM images and ED patterns, as illustrated in Figure 3. After lithiation, the NR in Figure 3a–d (Movie S3, Supporting Information) with a uniform diameter of 48 nm expands by 14.3% within 53 s, which is in accordance with the observations in Figure 2. It can be seen that the lattice fringes, corresponding to the (110) plane of H₂V₃O₈, still remain clear in the lithiated region, suggesting that the intercalation reaction mechanism dominates this lithiation stage. This is also reported by Gonjal et al. that the reversible intercalation

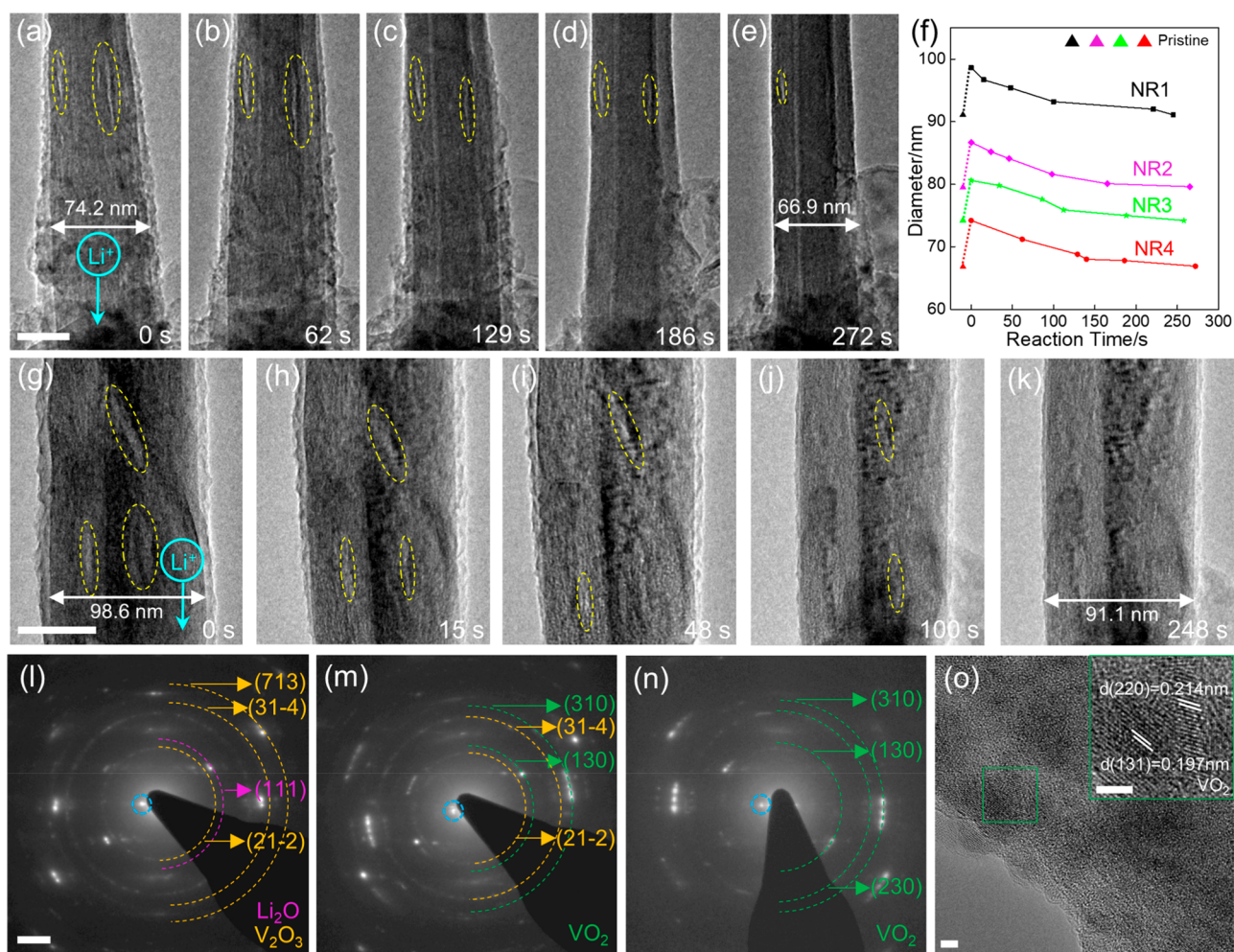


Figure 4. (a–e;g–k) Microstructure evolutions of the $\text{H}_2\text{V}_3\text{O}_8$ NR during the first delithiation process. The yellow outlines highlight the visible fissure domains upon the delithiation process. Scale bar, 50 nm. (f) Measured relationship between diameters and the delithiation time. (l–n) ED patterns used for identifying the phase evolution in the first electrochemical delithiation process. Scale bar, 2 1/nm. (o) Ex situ TEM images of $\text{H}_2\text{V}_3\text{O}_8$ at the delithiation state at 100 mA g⁻¹. Scale bar, 2 nm.

reaction can be maintained for $\text{H}_2\text{V}_3\text{O}_8$ within five Li's per formula unit (480 mAh g⁻¹).⁴¹ The intercalation of lithium ions directly leads to the fluctuation in the (110) lattice, as reflected by the FFT patterns in Figure 3a–d. The interplanar spacings of the (110) plane at different lithiation stages are obtained and are plotted as a function of lithiation time in Figure 3e. One can find that $\text{H}_2\text{V}_3\text{O}_8$ NRs undergo obvious “lattice breathing” that the d_{110} decreases slightly in the initial stage and subsequently increases.^{28,42} Similar lattice breathing is also found for other NRs, as shown in Figure 3e. The shrinkage of d spacing is caused by the strong interaction between the positively charged Li^+ and V_3O_8 bilayers. Subsequently, the slight increase in d spacing is attributed to the intercalation of more Li^+ , which expands the interlayer spacing.⁴² We note that during the first lithiation structural fissures with low contrast are also formed in $\text{H}_2\text{V}_3\text{O}_8$ NRs (Figures 3a–d and S4a–c and Movie S4, Supporting Information). They gradually grow larger in both longitudinal and lateral directions as the lithiation proceeds, finally evolving into ellipse shape. These structural fissures have their length directions basically parallel to the NR axes, as verified by three as-formed fissures in Figure 3d. The statistics of the angles between the fissures and NR axis are shown in Figure 3f. Obviously, most of the angles are in the range from 0 to 10°.

No distinct lattice fringes are observed in the region of fissures, which may suggest a different lithiation level other than the intercalation.

To deeply understand the fundamental reaction mechanisms during lithiation of $\text{H}_2\text{V}_3\text{O}_8$, time-lapsed ED patterns are arrayed in the order of Li^+ content from low to high in Figure 3g–i. The original $\text{H}_2\text{V}_3\text{O}_8$ NR shows an obvious single-crystalline feature (Figure 3g), in which the diffraction spots marked by blue dotted rings can be indexed as the (111) and (011) planes of the $\text{H}_2\text{V}_3\text{O}_8$ phase. Upon initial lithiation, the diffraction spots belonging to the initial $\text{H}_2\text{V}_3\text{O}_8$ phase basically remain, but new diffraction rings corresponding to the VO_2 phase (JCPDS No. 25-1003) and Li_2O phase (JCPDS No. 73-0593) are detected, as shown in Figure 3h. With further lithiation, Figure 3i reveals the presence of new diffraction rings belonging to the V_2O_3 phase (JCPDS No. 39-0774). In addition, it is found that some lattice fringes belonging to the $\text{H}_2\text{V}_3\text{O}_8$ phase could still be observed in Figure 3d, which indicates that the $\text{H}_2\text{V}_3\text{O}_8$ NRs cannot reach full conversion. In other words, the intercalation reaction and conversion reaction coexist after full lithiation. Combining the above HRTEM observation and ED analysis, we can infer that the conversion reaction should occur only in the region of fissures in lithiated NRs, considering the fact that other regions in NRs still remain

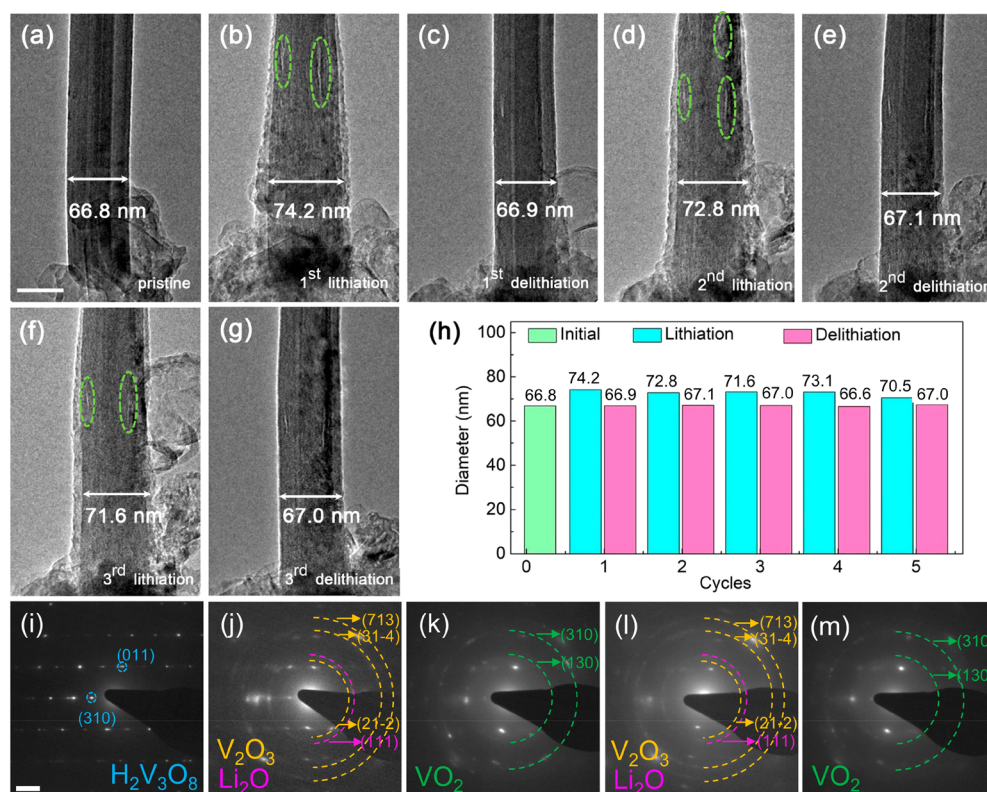


Figure 5. (a–g) Microstructure evolutions of the H₂V₃O₈ NR in the electrochemical lithiation/delithiation cycle processes. Scale bar, 50 nm. (h) Measured diameters versus electrochemical cycling times of the H₂V₃O₈ NR. The numeric percentages are for the diameter expansion/contraction during each event. (i–m) ED patterns of the first (i–k) and the second (l–m) lithiation/delithiation products to identify the overall reaction mechanism of H₂V₃O₈ in LIBs. Scale bar, 5 1/nm.

lattice fringes. The possible reactions involved during the first lithiation process are described as follows: H₂V₃O₈ → Li_xH₂V₃O₈ → VO₂ + Li₂O → V₂O₃ + Li₂O. Note that the scattering power and the structural factor of the H atom are very small, and its position is difficult to determine; therefore, the influence of the H atom can be ignored in the case of ED.²⁸

EELS white lines of transition metals, which include rich information about the density of unoccupied states near the Fermi level, can be used to quantitatively analyze the chemical element. Here, the difference in energy onset between the oxygen K edge and the transition metal V-L_{2,3} edges of oxides from the partially lithiated NR are obtained and given in Figure 3j. Generally speaking, these L₃ edge onset energies show a monotonic increase with cation oxidation state. For the V oxides, H₂V₃O₈ (V^{4.67+}) and VO₂ (V⁴⁺) are used as valence standard, and the relationship can be fitted linearly, $E_{L3} = a \cdot V_V + b$, with $a = 1.49$ and $b = 514.24$.⁴³ Initially, the average oxidation state of vanadium is +4.67. After the first lithiation process, the value can be estimated as +3.06 from the linear relationship, which is nearly approximate to V₂O₃(+3), corroborating the TEM results. A coin cell with H₂V₃O₈ NRs as the working electrode has also been conducted to verify the lithiated products after discharging at 0.2 V (vs Li⁺/Li). Figure S5 shows that the NR morphology remains integrated after discharging. Further, Figure 3k shows the corresponding high-resolution TEM images and FFT patterns. The lattice fringes are observed with *d*-spacings of 0.245 and 0.251 nm, agreeing with the (41–2) and (120) planes of V₂O₃, respectively. Similar results are also found when the H₂V₃O₈ NRs are discharged at the potential down to 1 V vs Li⁺/Li

(Figure S6). All of these findings fully confirm the phase transformations in above-mentioned conversion reactions during the first lithiation process.

During delithiation, a constant positive potential was applied on the already lithiated H₂V₃O₈ NRs with respect to the lithium counter electrode. Figure 4a–e,g–k (Movies S5 and S6, Supporting Information) show the electrochemical delithiation behaviors of lithiated H₂V₃O₈ NRs. With the extraction of lithium ions, the diameter of the lithiated NR in Figure 4g–k gradually shrinks from 98.6 to 91.1 nm within 248 s, resulting in a contraction of 7.6%. Moreover, it is found that the diameter shrinkage is about 9.8% for another NR in Figure 4a–e. Interestingly, we find that the delithiation process is accompanied by the disappearance of the fissures. Figure 4f shows the diameter changes of several NRs as a function of delithiation time, and the NRs all exhibit a similar tendency that the diameter shrinks first rapidly and then slowly. The Li₂O layers on the surface of the H₂V₃O₈ NRs also vanish. The ED patterns of delithiated NR were also recorded to identify phase evolutions, as displayed in Figure 4l–n. Upon delithiation, the diffraction rings attributed to V₂O₃ and Li₂O phases gradually disappear and the VO₂ phase is detected as the finally delithiated product, indicating that the delithiation process is an asymmetric reaction relative to the first lithiation process. However, it is found that periodic diffraction spots of H₂V₃O₈ are still visible. A coin cell with H₂V₃O₈ NRs after charging at 100 mA g⁻¹ has also verified the VO₂ phase as the delithiated product, as revealed in Figure 4o. In addition, no fissures are formed in the ex situ sample. In a way, we can speculate that the breathing fissures may be transient and

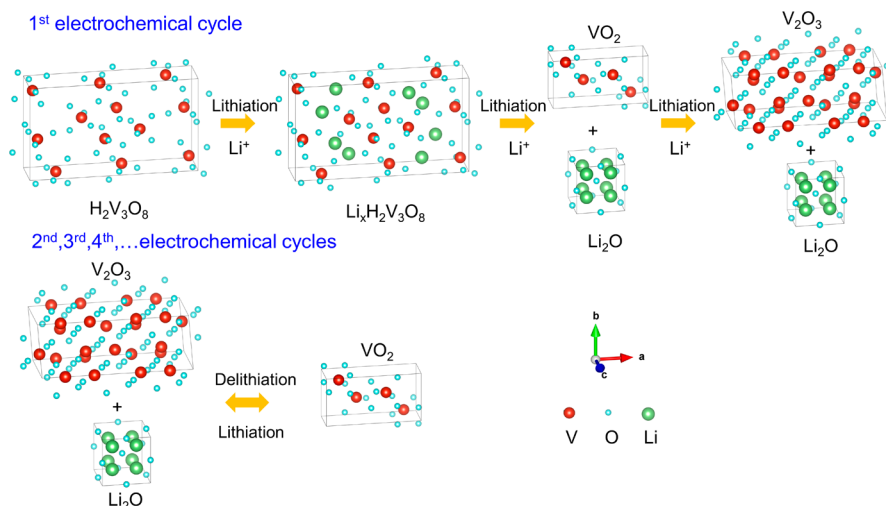


Figure 6. Schematic illustration of the conversion mechanism of the $\text{H}_2\text{V}_3\text{O}_8$ material during its first and subsequent electrochemical lithiation/delithiation cycles.

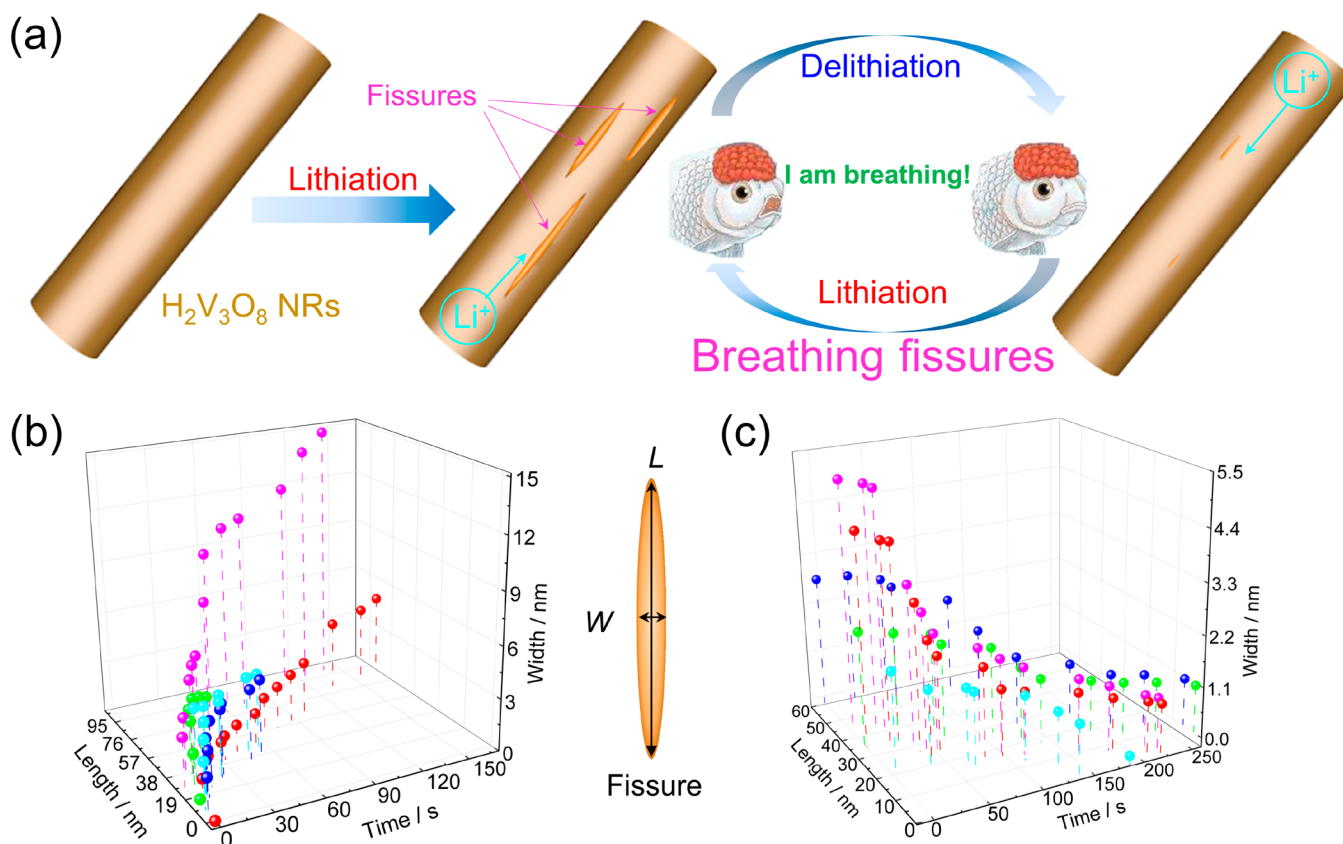


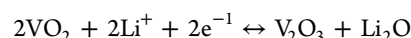
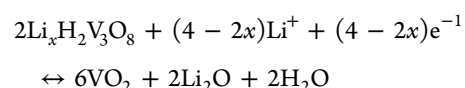
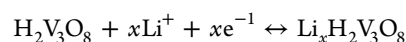
Figure 7. (a) Schematic illustration of the “breathing fissure” occurring in the $\text{H}_2\text{V}_3\text{O}_8$ NR upon (de)lithiation. The breathing fissure is like a mouth by which a goldfish breathes. The length and width of some fissures during (b) lithiation and (c) delithiation processes are plotted as a function of time.

happen only in the (de)lithiation process. For these reasons, the breathing fissures have not been found so far, indicating that in situ TEM is powerful for probing new phenomena in battery electrode materials.

To further demonstrate long-term structural restorability of $\text{H}_2\text{V}_3\text{O}_8$, electrochemical lithiation and delithiation cycles have been performed. As displayed in Figure 5 (Movie S6, Supporting Information), the $\text{H}_2\text{V}_3\text{O}_8$ NR exhibits multiple reversible volume expansions and contractions with the

insertion and extraction of lithium ions (Figure 5a–g). Figure 5h further displays the specific diameters for each cycle. From Figure 5a–h, we can see that the $\text{H}_2\text{V}_3\text{O}_8$ NR could nearly retain a similar size, and the fissures are also self-healing. These results demonstrate that the $\text{H}_2\text{V}_3\text{O}_8$ NR as an electrode material is viable for recyclable LIBs. Figure 5i–m presents the ED patterns of the $\text{H}_2\text{V}_3\text{O}_8$ NR during the first two cycles. It can be seen that the lithiated products can always be well indexed to V_2O_3 and Li_2O , which are further converted into

VO₂ after the first delithiation process. It is worth noting that the initial H₂V₃O₈ periodic diffraction spots are always present during the entire cycles, indicating the coexistence of the conversion and intercalation mechanisms. In addition, the ED patterns of the second (de)lithiated products indicated that the subsequent electrochemical cycles are reversible between the VO₂ and V₂O₃ phases, rather than the original H₂V₃O₈ phase. The EELS spectra collected at the fissures further proved the valence variation of element V during the first two cycles, as shown in Figure S7. The asymmetric phase transformation could result in irreversible capacity loss in the initial cycle, as indicated by the electrochemical discharge–charge cycle tests in Figure S8. In situ XRD measurement was also applied to further investigate the structural evolution of the H₂V₃O₈ electrode during the lithiation process. As shown in Figure S9, when the electrode discharges to 0.5 V (vs Li⁺/Li) for deep lithiation, reflections corresponding to (020), (520), and (511) peaks are observed with a slight shift, which indicates that the intercalation mechanism is the dominant reaction during deep lithiation of H₂V₃O₈. Consequently, the whole lithiation and delithiation reactions of H₂V₃O₈ NR can be expressed by the following equations and also can be visualized in Figure 6.



The schematic diagram of the breathing fissures during repeated lithiation and delithiation cycles is illustrated in Figure 7a. We use the breath of a goldfish to vividly delineate the evolution of the breathing fissures, as inset in Figure 7a. To probe the extension and shrinkage dynamics of the fissures in NRs, the length and width of some fissures during lithiation and delithiation are plotted as a function of time, as shown in Figure 7b,c, respectively. According to the statistical results, we find that the fissures grow initially quickly and then slowly during the lithiation. However, in the case of the delithiation, the fissures initially do not respond to the delithiation immediately. With further extraction of Li ions, the fissures shrink rapidly and gradually self-heal. It is believed that a certain amount of energy is required for phase transformations at the initial stages. On the basis of the above discussions, we believe that the local phase transformations result in the accumulation of internal stress in NRs during lithiation, which in turn leads to the generation of fissures at the grain boundary or defect sites.⁴⁴ Previous works have affirmed that such structural fissures are considered one of main reasons for degrading of the electrode materials. On the one hand, the fissures can lead to poor electrical conductivity, poor intergranular connections, and loss of active materials due to fragmentation. On the other hand, the fissures create fresh surfaces that will be exposed to electrolytes and generate new sites for surface phase transformation, corrosion, and side reactions, thus accelerating battery degradation.^{44,45} However, the fissures here in H₂V₃O₈ associated with conversion reactions are repairable, which has been corroborated by in situ TEM observations during repeated electrochemical cycles. In short, we for the first time not only clarify the conversion reaction in H₂V₃O₈ but also show the self-healing behavior of the fissures in this material. These insights and understanding

would provide important guidance to make H₂V₃O₈ a promising electrode for advanced rechargeable batteries.

In conclusion, the electrochemical lithiation and delithiation behaviors of H₂V₃O₈ NRs have been investigated by an in situ TEM approach. Upon initial lithiation, the orthorhombic H₂V₃O₈ follows an intercalation mechanism, and subsequent lithiation results in a localized intermediate VO₂ phase that is further converted into the V₂O₃ phase, accompanied by small volume expansion. Moreover, large structural fissures are formed in H₂V₃O₈ NRs during lithiation. During delithiation, the V₂O₃ phase is transformed into the VO₂ phase, rather than the original H₂V₃O₈ phase. Such a localized phase transformation between the VO₂ phase and V₂O₃ + Li₂O phases is reversible during subsequent cycles. Meanwhile, the fissures could appear and disappear alternately. Our findings provide an in-depth understanding of the electrochemical mechanism of H₂V₃O₈ NRs during the whole process of lithiation and delithiation, with the hope of assistance in designing LIBs with improved performance.

■ ASSOCIATED CONTENT

Supporting Information

The Supporting Information is available free of charge on the ACS Publications website at DOI: 10.1021/acseenergylett.9b01381.

Movie showing a lithiation segment where reaction fronts inside of single-crystalline H₂V₃O₈ NR propagated along the longitudinal direction (MP4)

Movie showing a lithiation segment of another H₂V₃O₈ NR (MP4)

Movie showing a high-resolution lithiation process of an individual H₂V₃O₈ NR (MP4)

Movie showing a high-resolution lithiation process of another H₂V₃O₈ NR (MP4)

Movie showing microstructure evolutions of H₂V₃O₈ NR in the first delithiation processes (MP4)

Movie showing microstructure evolutions of an individual single-crystalline H₂V₃O₈ NR in the first four electrochemical lithiation/delithiation processes (MP4)

Experimental details; crystal structure and XPS spectrum of core level V 2p of H₂V₃O₈, TEM images without electron beam irradiation and high-resolution TEM images of H₂V₃O₈ NR in the first lithiation process, and low-magnification TEM image of H₂V₃O₈ NR obtained from coin-type half cells after discharging at 0.2 V (PDF)

■ AUTHOR INFORMATION

Corresponding Authors

*E-mail: slt@seu.edu.cn (L.T.S).

*E-mail: mlq518@whut.edu.cn (L.Q.M).

*E-mail: fxu@seu.edu.cn (F.X.).

ORCID

Pengcheng Liu: 0000-0002-9530-9267

Shize Yang: 0000-0002-0421-006X

Peng Gao: 0000-0003-0860-5525

Litao Sun: 0000-0002-2750-5004

Liqiang Mai: 0000-0003-4259-7725

Feng Xu: 0000-0001-7738-9673

Author Contributions

*Y.W., X.M.X., and C.Y.Z. contributed equally.

Notes

The authors declare no competing financial interest.

ACKNOWLEDGMENTS

This work was supported by the National Natural Science Foundation of China (11774051, 61574034, 11774052, 11525415, and 51420105003), the 973 Program (2015CB352106), the Fundamental Research Funds for the Central Universities (2242018k1G012), the Scientific Research Foundation of Graduate School of Southeast University (YBJJ1661), the China Postdoctoral Science Foundation Funded Project (2014M550259, 2015T80480), and Jiangsu Planned Projects for Postdoctoral Research Funds (1401006A).

REFERENCES

- (1) Mai, L. Q.; Wei, Q. L.; An, Q. Y.; Tian, X. C.; Zhao, Y. L.; Xu, X.; Xu, L.; Chang, L.; Zhang, Q. J. Nanoscroll Buffered Hybrid Nanostructural VO₂(B) Cathodes for High-Rate and Long-Life Lithium Storage. *Adv. Mater.* **2013**, *25*, 2969–2973.
- (2) Ding, Y.-L.; Wen, Y.; Wu, C.; van Aken, P. A.; Maier, J.; Yu, Y. 3D V₆O₁₃ Nanotextiles Assembled from Interconnected Nanogrooves as Cathode Materials for High-Energy Lithium Ion Batteries. *Nano Lett.* **2015**, *15*, 1388–1394.
- (3) Zhang, L.; Zhao, K. N.; Luo, Y. Z.; Dong, Y. F.; Xu, W. W.; Yan, M. Y.; Ren, W. H.; Zhou, L.; Qu, L. B.; Mai, L. Q. Acetylene Black Induced Heterogeneous Growth of Macroporous CoV₂O₆ Nanosheet for High-Rate Pseudocapacitive Lithium-Ion Battery Anode. *ACS Appl. Mater. Interfaces* **2016**, *8*, 7139–7146.
- (4) Scrosati, B.; Hassoun, J.; Sun, Y. K. Lithium-Ion Batteries. A Look into the Future. *Energy Environ. Sci.* **2011**, *4*, 3287–3295.
- (5) Barpanda, P.; Nishimura, S. I.; Yamada, A. High-Voltage Pyrophosphate Cathode. *Adv. Energy Mater.* **2012**, *2*, 841–859.
- (6) Chu, S.; Majumdar, A. Opportunities and Challenges for a Sustainable Energy Future. *Nature* **2012**, *488*, 294–303.
- (7) Mai, L. Q.; Tian, X. C.; Xu, X.; Chang, L.; Xu, L. Nanowire Electrodes for Electrochemical Energy Storage Devices. *Chem. Rev.* **2014**, *114*, 11828–11862.
- (8) Cheng, F. Y.; Liang, J.; Tao, Z. L.; Chen, J. Functional Materials for Rechargeable Batteries. *Adv. Mater.* **2011**, *23*, 1695–1715.
- (9) Zhang, L.; Zhao, K. N.; Xu, W. W.; Dong, Y. F.; Xia, R.; Liu, F. N.; He, L.; Wei, Q. L.; Yan, M. Y.; Mai, L. Q. Integrated SnO₂ Nanorod Array with Polypyrrole Coverage for High-rate and Long-life Lithium Batteries. *Phys. Chem. Chem. Phys.* **2015**, *17*, 7619–7623.
- (10) Legagneur, V.; Le Gal La Salle, A.; Verbaere, A.; Piffard, Y.; Guyomard, D. Lithium Insertion/Deinsertion Properties of New Layered Vanadium Oxides Obtained by Oxidation of the Precursor H₂V₃O₈. *Electrochim. Acta* **2002**, *47*, 1153–1161.
- (11) Whittingham, M. S.; Song, Y.; Lutta, S.; Zavalij, P. Y.; Chernova, N. A. Some Transition Metal (oxy)Phosphates and Vanadium Oxides for Lithium Batteries. *J. Mater. Chem.* **2005**, *15*, 3362–3379.
- (12) Pang, H. C.; Cheng, P.; Yang, H. B.; Lu, J. L.; Guo, C. X.; Ning, G. L.; Li, C. M. Template-Free Bottom-Up Synthesis of Yolk-Shell Vanadium Oxide as High Performance Cathode for Lithium Ion Batteries. *Chem. Commun.* **2013**, *49*, 1536–1538.
- (13) Pan, A. Q.; Zhang, J. G.; Nie, Z. M.; Cao, G. Z.; Arey, B. W.; Li, G. S.; Liang, S. Q.; Liu, J. Facile Synthesized Nanorod Structured Vanadium Pentoxide for High-Rate Lithium Batteries. *J. Mater. Chem.* **2010**, *20*, 9193–9199.
- (14) Sarkar, A.; Sarkar, S.; Sarkar, T.; Kumar, P.; Bharadwaj, M. D.; Mitra, S. Rechargeable Sodium-Ion Battery: High-Capacity Ammonium Vanadate Cathode with Enhanced Stability at High Rate. *ACS Appl. Mater. Interfaces* **2015**, *7*, 17044–17053.
- (15) Ban, C.; Chernova, N. A.; Whittingham, M. S. Electrospun Nano-Vanadium Pentoxide Cathode. *Electrochem. Commun.* **2009**, *11*, 522–525.
- (16) Muster, J.; Kim, G. T.; Krstić, V.; Park, J. G.; Park, Y. W.; Roth, S.; Burghard, M. Electrical Transport Through Individual Vanadium Pentoxide Nanowires. *Adv. Mater.* **2000**, *12*, 420–424.
- (17) Watanabe, T.; Ikeda, Y. J.; Ono, T.; Hibino, M.; Hosoda, M.; Sakai, K. J.; Kudo, T. Characterization of Vanadium Oxide Sol as a Starting Material for High Rate Intercalation Cathodes. *Solid State Ionics* **2002**, *151*, 313–320.
- (18) Sarkar, S.; Bhowmik, A.; Pan, J.; Bharadwaj, M. D.; Mitra, S. Preparation, Structure Study and Electrochemistry of Layered H₂V₃O₈ Materials: High Capacity Lithium-Ion Battery Cathode. *J. Power Sources* **2016**, *329*, 179–189.
- (19) Liu, Z. W.; Xu, R. X.; Wei, W.; Jing, P.; Li, X.; Zhu, Q. Y.; Sun, H. J.; Dong, Y. Y.; Zakharova, G. S. Flexible H₂V₃O₈ Nanobelts/Reduced Graphene Oxide Electrodes with High Mass Loading for Lithium Ion Batteries. *Solid State Ionics* **2019**, *329*, 74–81.
- (20) Gao, S. K.; Chen, Z. J.; Wei, M. D.; Wei, K. M.; Zhou, H. S. Single Crystal Nanobelts of V₃O₇·H₂O: A Lithium Intercalation Host. *Electrochim. Acta* **2009**, *54*, 1115–1118.
- (21) Wang, D.; Wei, Q. L.; Sheng, J. Z.; Hu, P.; Yan, M. Y.; Sun, R. M.; Xu, X. M.; An, Q. Y.; Mai, L. Q. Flexible Additive Free H₂V₃O₈ Nanowire Membrane as Cathode for Sodium Ion Batteries. *Phys. Chem. Chem. Phys.* **2016**, *18*, 12074.
- (22) Xu, J.; Sun, H. J.; Li, Z. L.; Lu, S.; Zhang, X. Y.; Jiang, S. S.; Zhu, Q. Y.; Zakharova, G. S. Synthesis and Electrochemical Properties of Graphene/V₂O₅ Xerogels Nanocomposites as Supercapacitor Electrodes. *Solid State Ionics* **2014**, *262*, 234–237.
- (23) Zhang, C. P.; Song, H. Q.; Zhang, C. K.; Liu, C. F.; Liu, Y. G.; Cao, G. Z. Interface Reduction Synthesis of H₂V₃O₈ Nanobelts-Graphene for High-Rate Li-Ion Batteries. *J. Phys. Chem. C* **2015**, *119*, 11391–11399.
- (24) Liu, P. C.; Zhu, K. J.; Gao, Y. F.; Luo, H. J.; Lu, L. Recent Progress in the Applications of Vanadium-Based Oxides on Energy Storage: from Low-Dimensional Nanomaterials Synthesis to 3D Micro/Nano-Structures and Free-Standing Electrodes Fabrication. *Adv. Energy Mater.* **2017**, *7*, 1700547.
- (25) Liu, P. C.; Bian, K.; Zhu, K. J.; Xu, Y.; Gao, Y. F.; Luo, H. J.; Lu, L.; Wang, J.; Liu, J.; Tai, G. A. Ultrathin Nanoribbons of in Situ Carbon-Coated V₃O₇·H₂O for High-Energy and Long-Life Li-Ion Batteries: Synthesis, Electrochemical Performance, and Charge-Discharge Behavior. *ACS Appl. Mater. Interfaces* **2017**, *9*, 17002–17012.
- (26) He, P.; Quan, Y. L.; Xu, X.; Yan, M. Y.; Yang, W.; An, Q. Y.; He, L.; Mai, L. Q. High-Performance Aqueous Zinc-Ion Battery Based on Layered H₂V₃O₈ Nanowire Cathode. *Small* **2017**, *13*, 1702551.
- (27) Tang, H.; Xu, N.; Pei, C. Y.; Xiong, F. Y.; Tan, S. S.; Luo, W.; An, Q. Y.; Mai, L. Q. H₂V₃O₈ Nanowires as High-Capacity Cathode Materials for Magnesium-Based Battery. *ACS Appl. Mater. Interfaces* **2017**, *9*, 28667–28673.
- (28) Pang, Q.; Sun, C. L.; Yu, Y. H.; Zhao, K. N.; Zhang, Z. Y.; Voyles, P. M.; Chen, G.; Wei, Y. J.; Wang, X. D. H₂V₃O₈ Nanowire/Graphene Electrodes for Aqueous Rechargeable Zinc Ion Batteries with High Rate Capability and Large Capacity. *Adv. Energy Mater.* **2018**, *8*, 1800144.
- (29) Rastgoo-Deylami, M.; Chae, M. S.; Hong, S.-T. H₂V₃O₈ as a High Energy Cathode Material for Nonaqueous Magnesium-Ion Batteries. *Chem. Mater.* **2018**, *30*, 7464–7472.
- (30) Huang, J. Y.; Zhong, L.; Wang, C. M.; Sullivan, J. P.; Xu, W.; Zhang, L. Q.; Mao, S. X.; Hudak, N. S.; Liu, X. H.; Subramanian, A.; Fan, H. Y.; Qi, L. A.; Kushima, A.; Li, J. In Situ Observation of the Electrochemical Lithiation of a Single SnO₂ Nanowire Electrode. *Science* **2010**, *330*, 1515–1520.
- (31) McDowell, M. T.; Ryu, I.; Lee, S. W.; Wang, C.; Nix, W. D.; Cui, Y. Studying the Kinetics of Crystalline Silicon Nanoparticle Lithiation with In Situ Transmission Electron Microscopy. *Adv. Mater.* **2012**, *24*, 6034–6041.
- (32) Gu, M.; Kushima, A.; Shao, Y.; Zhang, J.-G.; Liu, J.; Browning, N. D.; Li, J.; Wang, C. Probing the Failure Mechanism of SnO₂ Nanowires for Sodium-Ion Batteries. *Nano Lett.* **2013**, *13*, 5203–5211.

(33) Xia, W. W.; Zhang, Q. Z.; Xu, F.; Sun, L. T. New Insights into Electrochemical Lithiation/Delithiation Mechanism of α - MoO_3 Nanobelt by in Situ Transmission Electron Microscopy. *ACS Appl. Mater. Interfaces* **2016**, *8*, 9170–9177.

(34) Xu, F.; Li, Z. R.; Wu, L. J.; Meng, Q. P.; Xin, H. L.; Sun, J.; Ge, B. H.; Sun, L. T.; Zhu, Y. M. In situ TEM Probing of Crystallization Form-Dependent Sodiation Behavior in ZnO Nanowires for Sodium-Ion Batteries. *Nano Energy* **2016**, *30*, 771–779.

(35) Oka, Y.; Yao, T.; Yamamoto, N. Structure Determination of $\text{H}_2\text{V}_3\text{O}_8$ by Power X-Ray Diffraction. *J. Solid State Chem.* **1990**, *89*, 372–377.

(36) Sladek, N. E.; Mannering, G. J. Induction of Drug Metabolism. *Mol. Pharmacol.* **1969**, *5*, 174–185.

(37) Zhu, K.; Yan, X.; Zhang, Y. Q.; Wang, Y. H.; Su, A. Y.; Bie, X. F.; Zhang, D.; Du, F.; Wang, C. L.; Chen, G.; Wei, Y. G. Synthesis of $\text{H}_2\text{V}_3\text{O}_8$ /Reduced Graphene Oxide Composite as a Promising Cathode Material for Lithium-Ion Batteries. *ChemPlusChem* **2014**, *79*, 447–453.

(38) Simões, M.; Mettan, Y.; Pokrant, S.; Weidenkaff, A. Surface-Modified Lithiated $\text{H}_2\text{V}_3\text{O}_8$: A Stable High Energy Density Cathode Material for Lithium-Ion Batteries with LiPF_6 Electrolytes. *J. Phys. Chem. C* **2014**, *118*, 14169–14176.

(39) Van der Ven, A.; Thomas, J. C.; Xu, Q.; Swoboda, B.; Morgan, D. Nondilute Diffusion from First Principles: Li Diffusion in Li_xTiS_2 . *Phys. Rev. B: Condens. Matter Mater. Phys.* **2008**, *78*, 104306.

(40) Wang, J. W.; Liu, X. H.; Mao, S. X.; Huang, J. Y. Microstructural Evolution of Tin Nanoparticles during in Situ Sodium Insertion and Extraction. *Nano Lett.* **2012**, *12*, 5897–5902.

(41) Prado-Gonjal, J.; Molero-Sánchez, B.; Ávila-Brandé, D.; Morán, E.; Pérez-Flores, J. C.; Kuhn, A.; García-Alvarado, F. The Intercalation Chemistry of $\text{H}_2\text{V}_3\text{O}_8$ Nanobelts Synthesised by A Green, Fast and Cost-Effective Procedure. *J. Power Sources* **2013**, *232*, 173–180.

(42) Wei, Q. L.; Jiang, Z. Y.; Tan, S. S.; Li, Q. D.; Huang, L.; Yan, M. Y.; Zhou, L.; An, Q. Y.; Mai, L. Q. Lattice Breathing Inhibited Layered Vanadium Oxide Ultrathin Nanobelts for Enhanced Sodium Storage. *ACS Appl. Mater. Interfaces* **2015**, *7*, 18211–18217.

(43) Tan, H. Y.; Verbeeck, J.; Abakumov, A.; Van Tendeloo, G. Oxidation State and Chemical Shift Investigation in Transition Metal Oxides by EELS. *Ultramicroscopy* **2012**, *116*, 24–33.

(44) Yan, P. F.; Zheng, J. M.; Gu, M.; Xiao, J.; Zhang, J. G.; Wang, C. M. Intragranular Cracking as A Critical Barrier for High-Voltage usage of Layer-Structured Cathode for Lithium-Ion Batteries. *Nat. Commun.* **2017**, *8*, 14101.

(45) Yan, P. F.; Zheng, J. M.; Chen, T. W.; Luo, L. L.; Jiang, Y. Y.; Wang, K.; Sui, M. L.; Zhang, J. G.; Zhang, S. L.; Wang, C. M. Coupling of Electrochemically Triggered Thermal and Mechanical Effects to Aggravate Failure in A Layered Cathode. *Nat. Commun.* **2018**, *9*, 2437.